MEDICAL ROBOTS

Development of a magnetic microrobot for carrying and delivering targeted cells

Junyang Li[1,2]*, Xiaojian Li[1]*, Tao Luo[1], Ran Wang[1], Chichi Liu[3], Shuxun Chen[1], Dongfang Li[1], Jianbo Yue[3], Shuk-han Cheng[3], D. Sun[1,2]†

The precise delivery of targeted cells through magnetic field–driven microrobots/carriers is a promising technique for targeted therapy and tissue regeneration. This paper presents a microrobot designed with a burr-like porous spherical structure for carrying and delivering targeted cells in vivo under a magnetic gradient field–driven mechanism. The robot was fabricated by using three-dimensional laser lithography and coated with Ni for magnetic actuation and Ti for biocompatibility. Numerical and experimental studies demonstrated that the proposed microrobot design could enhance magnetic driving capability, promote cell-carrying capacity, and benefit cell viability. Microrobots loaded with cells could be automatically controlled to reach a desired site by using a self-constructed electromagnetic coil system, as verified by in vivo transport of cell-cultured microrobots in zebrafish embryos. The carried cells could be spontaneously released from the microrobot to the surrounding tissues; in vitro experiments showed that cells from the microrobot were directly released onto the desired site or were able to pass through the blood vessel–like microchannel to arrive at the delivery area. Further in vivo cell-releasing tests were performed on nude mice, followed by histological study. This research provides a microrobotic device platform for regenerative medicine and cell-based therapy.

INTRODUCTION

Regenerative medicine with cell-based therapy has obtained considerable attention in recent years (*1*, *2*). Stem cells, which are either derived from an autologous biopsy of a patient or reprogrammed from somatic cells, can differentiate into functional cells and be delivered to a damaged location for tissue function restoration (*3*–*8*). The delivery of such cells in vivo requires a suitable three-dimensional (3D) structure that creates an environment that supports cell adhesion, proliferation, and differentiation while functioning as a carrier (*9*, *10*). Producing a 3D cell culture environment is important for in vitro cell loading to allow in vivo–like behavior of resident cells in terms of cell morphology and function. By contrast, cells cultured in 2D substrates rapidly lose their function and morphology (*11*). For in situ regeneration, a microcarrier with a porous 3D structure can be used for cell adhesion and mechanical support for tissue and organ regeneration (*12*). This microcarrier stimulates the cells of the body to promote local tissue repair (*13*) and to produce sufficient nutrient supply and uniform cell distribution (*12*). The size of these cell carriers can vary by orders of magnitude. Large-scale cell carriers that are fabricated and implanted in tissue environment are invasive, may cause postoperative pain, and may increase infection risk and overall recovery time (*14*–*18*). Large-scale carriers can barely access the complex and small regions of the human body, such as gastrointestinal organs, brain, and spinal cord (*19*). The development of microrobots for minimally invasive medicine has considerably advanced (*20*, *21*). However, actuators that can be used for in vivo propelling of robots in microscale are still lacking (*22*). Currently, a viable option for steering such a microrobot is through external energy transfer.

Magnetic fields have gained much interest because of their advantages: insensitivity to biological substances, no direct contact, and precise positioning ability (*23*–*25*). Magnetic fields that are generated ex vivo for energy transfer and propulsion can provide a solution to the in vivo actuation problem. Several magnetic microcarrier devices have been developed and used for precise cell transport. Cell-encapsulating hydrogel combined with magnetic particles through integration with microfluidic chips (*26*) or ultraviolet photocrosslinking (*27*) can control and transport cells. A microtransporter with syringe-like shape has been developed to collect, transport, and release cell-loaded microparticles inside microfluidic channels (*28*). A U-shaped ferromagnetic microrobot driven by an external magnetic field could automatically manipulate cells and microbeads (*29*). Microrobots with helical and tubular lipid structures are used as cell delivery platforms with high propulsion efficiency (*30*, *31*). An alga-templated biodegradable magnetic helical swimming microrobot using both fluorescence and magnetic resonance imaging for imaging-guided therapy has been reported (*32*). Magnetic microrobots with 3D porous hexahedral and cylindrical shapes were designed with increased biocompatibility for the transport of multiple cells and have been demonstrated in vitro (*12*). Microrobots actuated by magnetic field may present many advantages in the application of in vitro cell delivery but may not reflect the complexity of in vivo situation inside multicellular organisms. A specifically designed magnetic microrobot that is based on actual needs in the body for carrying and delivering a group of cells has not yet been demonstrated.

This paper reports the design of a magnetically driven microrobot with a burr-like porous spherical structure that was fabricated using 3D laser lithography to achieve in vivo transport and delivery of targeted cells. Herein, the magnetic gradient field–driven mechanism was used so that the microrobot design was not constrained by the robot shape, providing flexibility in considering different robot structures for carrying cells. The microrobot was coated with Ni to achieve magnetic actuation and Ti to ensure biocompatibility. Both numerical and experimental studies were performed to demonstrate that the

---

[1]Department of Mechanical and Biomedical Engineering, City University of Hong Kong, Hong Kong SAR, China. [2]Centre for Robotics and Automation, Shenzhen Research Institute of City University of Hong Kong, Shenzhen 518057, China. [3]Department of Biomedical Sciences, City University of Hong Kong, Hong Kong SAR, China.
*These authors contributed equally to this work.
†Corresponding author. Email: medsun@cityu.edu.hk

proposed robot design could greatly enhance magnetic driving capability and benefit cell-carrying capacity. Viability tests performed on MC3T3-E1 fibroblasts and mesenchymal stem cells (MSCs) also demonstrated that the designed microrobot exhibited good cell loading and cultivation capacity. A microrobot with cultured cells could be automatically and precisely transported to a desired position, which was verified using a self-constructed electromagnetic coil setup (*33*). The in vivo transport of cell-cultured microrobots to a desired site in the yolks of zebrafish embryos was successfully performed. Zebrafish has been increasingly used as a vertebrate embryo model because of its genetic similarity to humans and transparent and relatively large yolk for microrobot transportation (*34*, *35*). In the current study, the cells carried by the designed microrobot could be spontaneously released from the microrobot to the desired site. This deduction was confirmed by conducting in vitro experiments to release cells from the microrobots to a glass substrate or to enable the cells to pass through a blood vessel–like microchannel to arrive at the delivery area. Further in vivo cell-releasing experiments from cell-cultured microrobots into nude mice were performed, followed by histological study. Results showed that the designed magnetic microrobots could successfully carry and deliver the targeted cells to a desired site. This precise delivery of targeted cells holds potential for numerous medical applications, such as targeted therapy, tissue repair, and regeneration.

RESULTS

Microrobot design

The designed microrobot uses a burr-like porous spherical structure to enhance magnetic driving and cell-carrying capabilities. Figure 1A shows the structural design of the microrobot before and after cell seeding. The distance between two burrs, which was denoted as the grid length (l_g), was determined on the basis of the size of the carried cells. The length of each burr, which was denoted as the burr length (l_b), was the same as the radius of cell (r_c). The diameter of the entire structure (D), including burrs, was determined according to l_g, l_b, r_c, and the radius of grid (r_g), which ranged from 70 to 90 μm for different cell types in the current study. Figure 1B illustrates the fabrication of the microrobot with steps of writing, development, Ni/Ti deposition, and cell culture on the robot. Both l_g and l_b could be adjusted by using 3D laser lithography to suit different cell types. Scanning electron microscopy (SEM) images of a microrobot (Fig. 1C) show where MC3T3-E1 cells and MSCs were successfully cultured onto the robot after 12 hours at a concentration of 1 × 10^6 cells/ml. The energy-dispersive spectrometry spectra of the Ni/Ti-coated substrate (fig. S1) confirmed the successful coating process. Justifications of this robot design are specified as follows.

First, a spherical structure can enhance magnetic driving capability, besides allowing easy fusion of the microrobot with host tissues and facilitating cell transfer from the robot to tissues (*36*–*38*). When the microrobot moves inside blood vessels, the magnetic field gradient force, which is proportional to the coating thickness and the cross-sectional area of the magnetically conductive materials that are coated on the robot surface, must be large enough to overcome viscous resistance. A numerical study using the finite element method was conducted on a 3D cubic geometry (*12*) and the proposed spherical structure, respectively, as illustrated in Fig. 2. In the simulations, 2D spiral and flat geometries were neglected because they are normally used for drug/gene loading by surface modification (*39*) or encapsulation inside of the geometry (*40*), which may not apply to a 3D cell culture structure. The maximum cross-sectional areas of the robots with the two different structures were the same for easy comparison. Under the same coating thickness, magnetic force increased as surface area increased, and an increased ratio of surface area to viscous resistance represented an enhanced magnetic driving capability. Therefore, the surface area–to–resistance ratio can be used as a criterion to judge magnetic driving capability. Similar to a previous study (*41*), the current study used blood vessels of hepatic artery, portal vein, and hepatic vein with 160-, 240-, and 320-μm diameters, respectively. The flow rate was uniformly set to 25 cm/s, which corresponds to

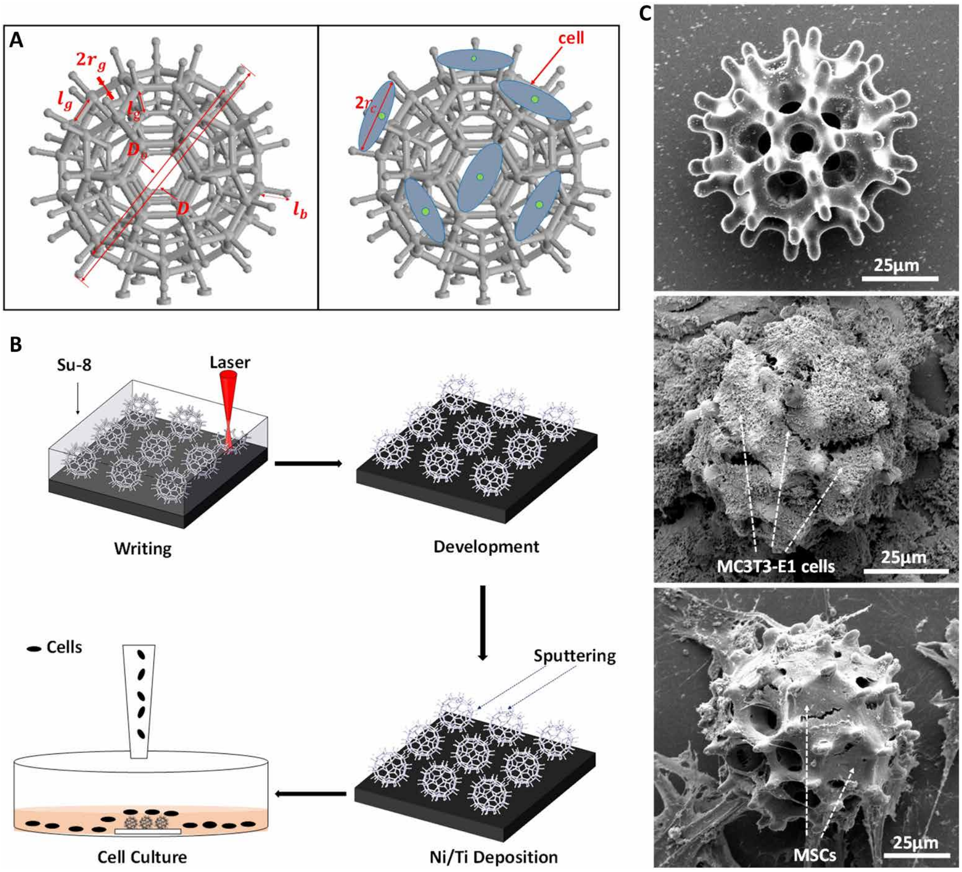

Fig. 1. Design and fabrication of magnetic microrobots. (**A**) Images of the designed burr-like porous spherical microrobot before and after cell seeding. (**B**) Fabrication procedures of the microrobots including writing, developing, Ni/Ti deposition, and cell culture process. (**C**) SEM images of a burr-like microrobot cultured with MC3T3-E1 cells and MSCs for 12 hours. The laser power and scan speed of photoresist were set at 25 mW and 250 μm/s, respectively.

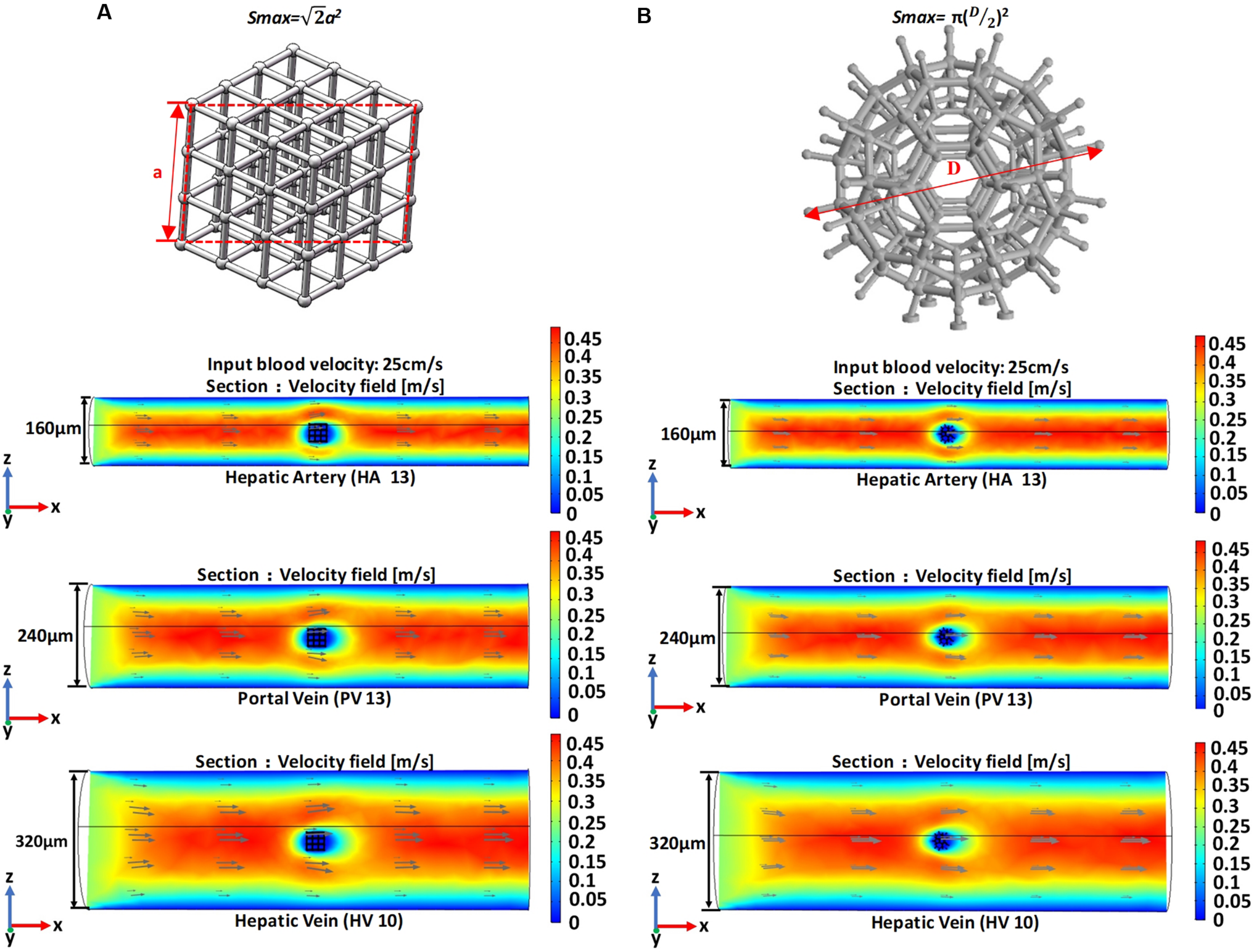

C

Ratios of surface area to viscous resistance of the structure(mm^2/N)

	HA 13 Diameter: 160μm	PV 13 Diameter: 240μm	HV 10 Diameter: 320μm
Cubic structure Side length : 37μm Surface area: 0.010mm^2	2801	3830	4315
Burr-like spherical structure Diameter: 50μm Surface area: 0.007mm^2	3478	4320	4665

Fig. 2. Simulation results of magnetic driving ability in hepatic artery, portal vein, and hepatic vein. (**A**) Velocity fields of a cubic structure. (**B**) Velocity fields of a burr-like spherical structure. (**C**) Surface area–to–viscous resistance ratios of the two microrobot structures.

the normal hepatic arterial and portal venous blood flow (*42*). Figure 2B illustrates the simulation results of the velocity fields in the cross-sectional areas of both cubic and spherical structures under different environments. The surface area–to–resistance ratios of the two structures are shown in Fig. 2C. The ratio for the proposed robot structure was higher than that of the cubic structure, implying that the designed robot with a spherical structure exhibited a stronger magnetic driving capability.

Second, a porous spherical structure can also improve cell-carrying capacity. The porous scaffold structure mimics the extracellular matrix, allowing the easy supply of nutrients for tissue vascularization to yield functional tissues and organs (*43*, *44*) and cell growth (*45*). The scaffold structure of fullerene, which is characterized by combinations of pentagons and hexagons in the grids, can benefit cellular attachment compared with a structure of triangles and squares (*46*). With such a porous scaffold, cell-loading capacity can be maximized when the grid length is similar to the radius of the carried cells. The size of an entire microrobot is mainly determined by the following two requirements in its application. The first requirement is effective cell loading; that is, the microrobot must have sufficiently large dimensions such that at least dozens of cells can be carried and delivered by each robot. The second requirement is efficient accessing ability. The microrobot must not be so large such that the cell-cultured robot cannot access various kinds of blood vessels; for instance, the mean diameter of the finest hepatic artery is 160 μm (*41*). To balance the above two requests, we selected the structure of a buckyball (C_{60}) for the proposed microrobot design, which exhibited an l_g–to–structure diameter (D_o) ratio of 1:4.8. The diameter of the entire designed microrobot was then determined as $D = D_o + 2l_b = 4.8(l_g + 2r_g) + 2r_g + 2l_b$.$l_g$ is a key parameter in determining cell-carrying capacity when the cell radius r_c is known. Figure 3A illustrates the experimental results of loading and culturing MC3T3-E1 cells ($r_c = 7.5$ μm) when $l_g = 0.8r_c$, r_c, $1.2r_c$, $1.4r_c$, $1.6r_c$, $1.8r_c$, where $l_b = r_c$ and the scaffold grid radius $r_g = 1$ μm. The microrobot exhibited the best cell-carrying capacity when $l_g = 1.2r_c$. With these selected parameters, the diameter of the microrobot was about 70 μm for carrying MC3T3-E1 cells. In a similar manner, the diameter of the microrobot was about 90 μm for carrying MSCs ($r_c = 10$ μm).

Third, the addition of a burr-like structure to the porous spherical microrobot can further enhance cell-carrying capacity. Spherical porous microrobots with different burr sizes were compared on the basis of the cell cultivation performance of microrobots that were fabricated on the same glass substrate (within 200 μm) with each microrobot carrying the same amount of cells for culture. Figure 3B illustrates the results of experiments performed on the MC3T3-E1 cells at $l_b = 0$, $0.5r_c$, r_c, $1.5r_c$, $2r_c$, $3r_c$, where $l_g = 1.2r_c$, which was based on the previous selection. The microrobot exhibited the best cell-loading capability when $l_b = r_c$.

Cell viability

The influence of the coating materials Ni and Ti on the cell culture was investigated. Viability tests were performed on MC3TE-E1 cells and MSCs, which were cultured on Ni- and Ti-coated flat square glasses. Cells cultured on clean glasses without Ni and Ti coatings were used as controls. Before cell seeding, the glass substrates were sterilized with ultraviolet light. SEM images captured on days 1, 3, and 5 of the MC3T3-E1 cells and MSCs cultured on the glass substrate are shown in Fig. 4 (A and B). After coating the glass surface with Ti, the cells exhibited good morphology and proliferated. The survival rates of two types of cells on days 1, 3, and 5 are illustrated in Fig. 4C. The negative and positive signs represent the propidium iodide (PI) region for live and dead cells, respectively. A histogram of the average viability of the two types of cells is presented in Fig. 4D. These data revealed that the Ni and Ti materials coated on the surface of the microrobots were not cytotoxic to MC3T3-E1 cells and MSCs, as evidenced by their ready adherence onto the robot structure and subsequent proliferation.

Transportation of the cell-cultured microrobot

First, experiments were performed on the in vitro transport of MC3T3-E1 cell–cultured microrobots ($D = 70$ μm) to reach a desired position,

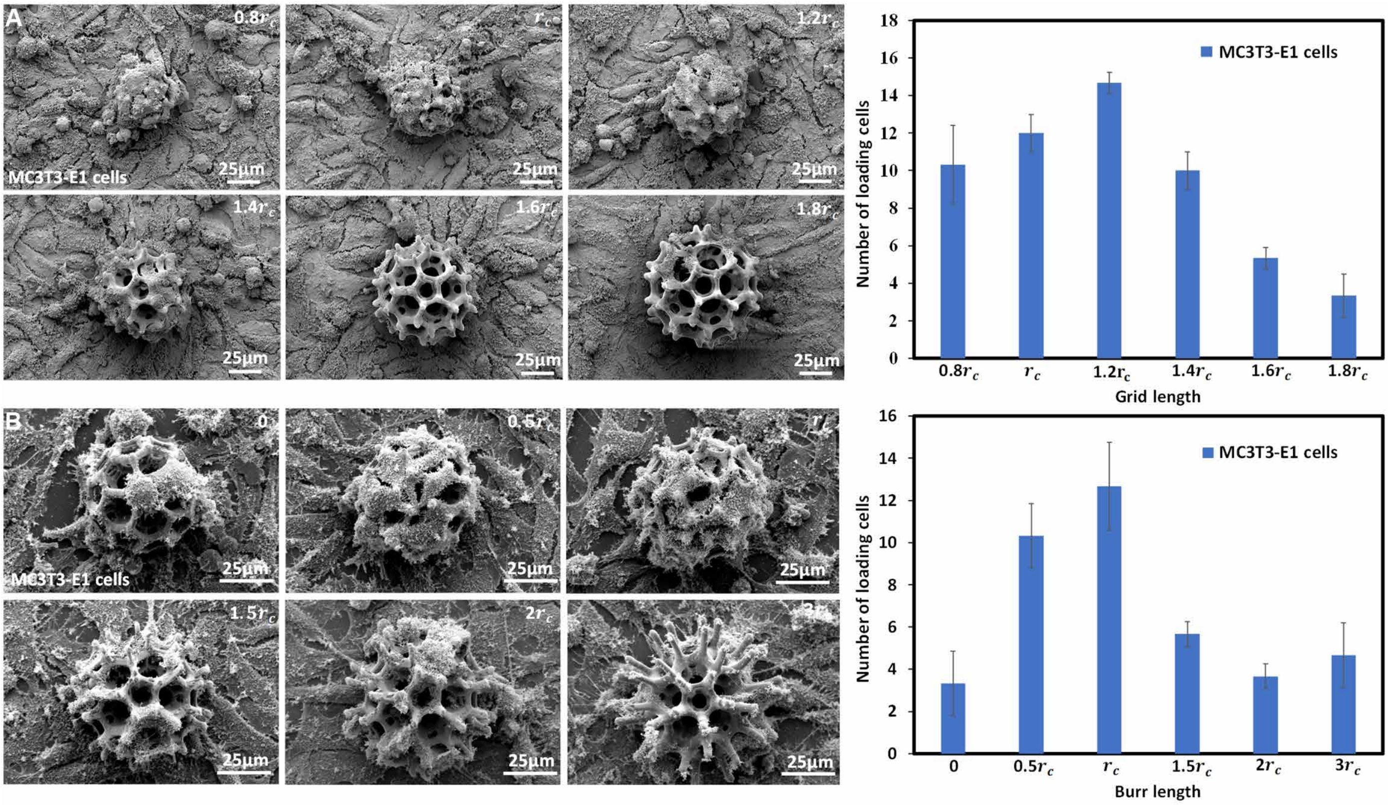

Fig. 3. Microrobots with different cell-carrying capacities under different grid lengths (l_g) and burr lengths (l_b). (**A**) SEM images and statistical results of cell-cultured microrobots when $l_g = 0.8r_c$, r_c, $1.2r_c$, $1.4r_c$, $1.6r_c$, $1.8r_c$, where r_c is the mean radius of carried cells ($n = 3$). (**B**) SEM images and statistical results of cell-cultured microrobots when $l_b = 0$, $0.5r_c$, r_c , $1.5r_c$, $2r_c$, $3r_c$ ($n = 3$). Error bars indicate SD.

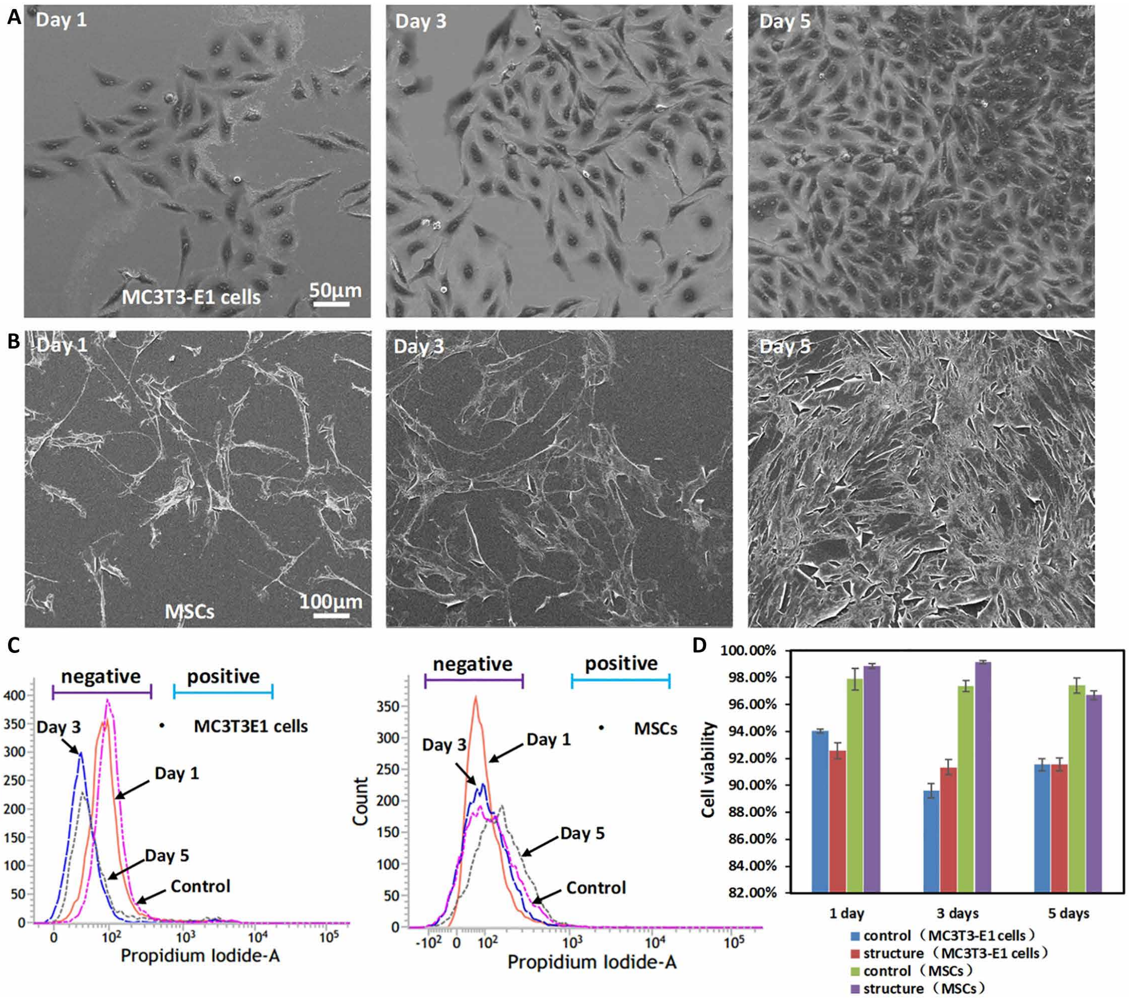

Fig. 4. Cell viability tests. SEM images of (**A**) MC3T3-E1 cells and (**B**) MSCs on days 1, 3, and 5 of culture. (**C**) Survival rates of MC3T3-E1 cells and MSCs in culture at 1, 3, and 5 days after PI staining. (**D**) Histogram representing the average viability of cells cultured for 1, 3, and 5 days ($n = 3$). Error bars indicate SD.

controlled by a visual feedback transportation controller as detailed in the Supplementary Materials. A self-constructed electromagnetic coil system, as shown in fig. S2, was used to drive the cell-cultured microrobot. A microrobot carrying cultured MC3T3-E1 cells moved along a rectangular path toward the four desired positions—a, b, c, and d—under a visual position feedback control (Fig. 5A). A phase-contrast image of the microrobot carrying MC3T3-E1 cells is also shown in Fig. 5A. Figure 5B shows that the translational velocity of the microrobot increased as the applied magnetic field gradient increased in a nearly linear relationship in three different fluid environments, including phosphate-buffered saline (PBS), artificial cerebrospinal fluid [140.0 mM NaCl/3.0 mM KCl/1.0 mM $MgCl_2$/1.3 mM $CaCl_2$/2.0 mM Na_2HPO_4/2.0 mM NaH_2PO_4/10.0 mM glucose (pH = 7.4)], and mouse blood serum (centrifuged for 3 min at 300*g* from 6-week-old Balb/C nude mouse). Increase of volume magnetization leads to increase of the moving velocity under the same magnetic gradient, which can be achieved by increasing the thickness of the coating materials (Ni) (*47*). The position errors of the cell-cultured microrobot converged to zero as it moved along a desired rectangle (Fig. 5C). In this experiment, the actual position of the robot was measured using an image processing technique that includes the three basic steps of threshold segmentation, connected region extraction, and positional correlation (*48*). All data were obtained by repeating the experiment at least thrice, and the Reynolds numbers and the related experimental parameters are given in table S1. The above-mentioned results verified that the designed microrobot with cultured cells could be automatically and precisely transported to a desired position using an electromagnetic coil setup.

Experiments on the in vivo transport of the MSC-cultured microrobot ($D = 90$ µm) were then performed in the yolks of 30-hour post-fertilization zebrafish embryos. Zebrafish has been widely used as an animal model because of its high genetic similarity to humans. The yolk of zebrafish is transparent for easy monitoring and sufficiently large for microrobot movement. The MSC-cultured microrobot was sucked by air pressure at the tip of a needle and injected into the yolk of an anesthetized zebrafish embryo (fig. S3). The MSC-cultured microrobot moved from a to b and then from b to c in the yolk of a zebrafish embryo at different time points (Fig. 5D). The heartbeat of the zebrafish could be observed during the experiment, indicating that the zebrafish was alive. The microrobot could not move until the magnetic field gradient was sufficiently large to overcome a threshold (Fig. 5E). Figure 5F illustrates the position error of the

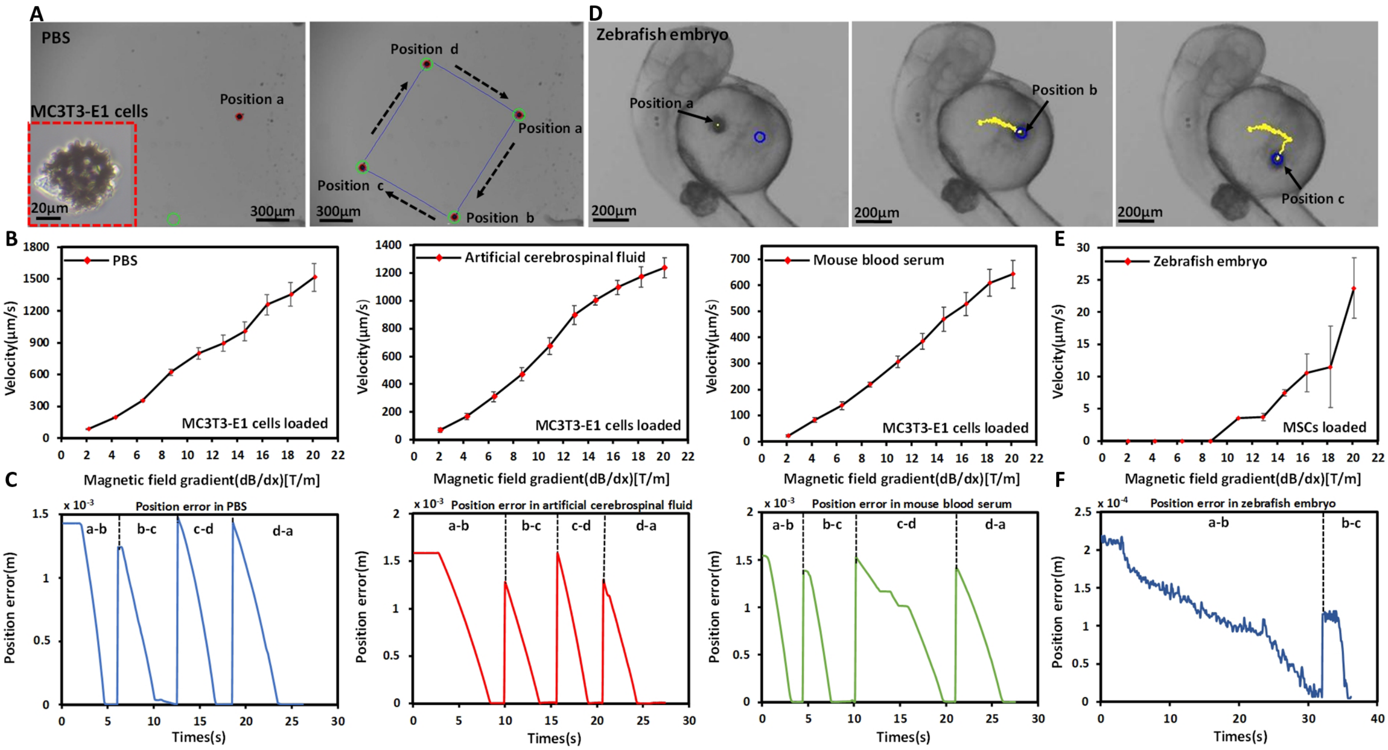

Fig. 5. Control of a cell-cultured microrobot in vitro and in vivo. (**A**) Movement of a microrobot cultured with MC3T3-E1 cells along a desired rectangular path in clockwise direction in PBS. (**B**) Velocity of MC3T3-E1 cell–cultured microrobot against the magnetic field gradient in different fluid environments ($n = 4$). (**C**) Position errors of the MC3T3-E1 cell–cultured microrobot in different fluid environments (with a magnetic field gradient of 4 to 9 T/m). (**D**) Time-lapsed images of the MSC-cultured microrobot moving in the yolk of a zebrafish embryo. (**E**) Velocity of MSC-cultured microrobot against the magnetic field gradient in vivo ($n = 4$). (**F**) Positional errors of the MSC-cultured microrobot in vivo (with a magnetic field gradient of 20 T/m). Error bars indicate SD.

robot. The velocity during interval a to b was lower than that during interval b to c because of different viscosities due to the presence of proteins, nucleic acids, and other bio-macromolecules in the yolk of zebrafish embryo. A dynamic analysis of a magnetic microrobot inside a zebrafish, as detailed in the Supplementary Materials, indicated that the velocity was about proportional to the magnetic field gradient, and the dynamic viscosity varied from 0.1219 to 0.3734 Pa·s in the yolk of zebrafish embryo. Compared with other living environments, such as PBS, artificial cerebrospinal fluid, or mouse blood serum, the yolk of zebrafish embryo exhibits higher viscosity, greater viscous resistance, and uneven material distribution. Consequently, the navigation speed of the microrobot was much slower in the zebrafish embryo than in the other media (Fig. 5B and fig. S4) under the same gradient force.

Delivery of cells from the microrobot to the site

After the microrobot with carried cells arrives at the desired site, the transfer of cells from the microrobot onto the site defines the successful cell delivery of the designed microrobot. We hypothesized that the cells can be spontaneously released from the microrobot onto the surrounding tissues, thereby leveraging the proposed microrobot structural design. To verify this idea, we first performed in vitro experiments on releasing cells from the microrobot onto a glass substrate. Figure 6A shows the phase-contrast images of the MC3T3-E1 cells that were carried by the microrobot, which was in contact with a pure glass substrate. After 1 day of cell culture, six 3T3 cells were released from the microrobot and firmly attached to the glass substrate. After 2 days of cell culture, the released 3T3 cells differentiated, 11 of which were found on the glass substrate. After 3 days of cell culture, 25 3T3 cells proliferated onto the substrate. These results confirmed the successful cell delivery from the microrobot and cell growth on the substrate in vitro. The microrobot carrying cultured MSCs was then placed onto a glass substrate with precultured C2C12 cells to simulate a microtissue environment (Fig. 6B). The MSCs carried by the microrobot were labeled with the fluorescent reagent carboxyfluorescein diacetate succinimidyl ester (CFDA SE) before they were released onto the substrate. After 7 days of cultivation, the labeled MSCs proliferated onto the substrate (Fig. 6B). These results again verified that the cells carried by the developed microrobot could be successfully transferred onto a desired site in vitro.

We secondly performed in vitro experiments involving the release of MC3T3-E1 cells from the microrobot in a microfluidic chip to mimic the transendothelial migration of the released cells. The chip consisted of blood vessel–like microchannels to mimic the vascular network, an array of cell migration channels to mimic the endothelial layer, and tissue chambers where the cells were delivered. Figure 7A illustrates a schematic of the experiment, where the cell-cultured microrobot was transferred along the microchannel to the docking area for releasing cells, and the released cells moved through migration channels and arrived in the tissue chambers. Figure 7B illustrates the experimental results of the transendothelial migration of MC3T3-E1 cells in 3 days. Some released cells were found in the

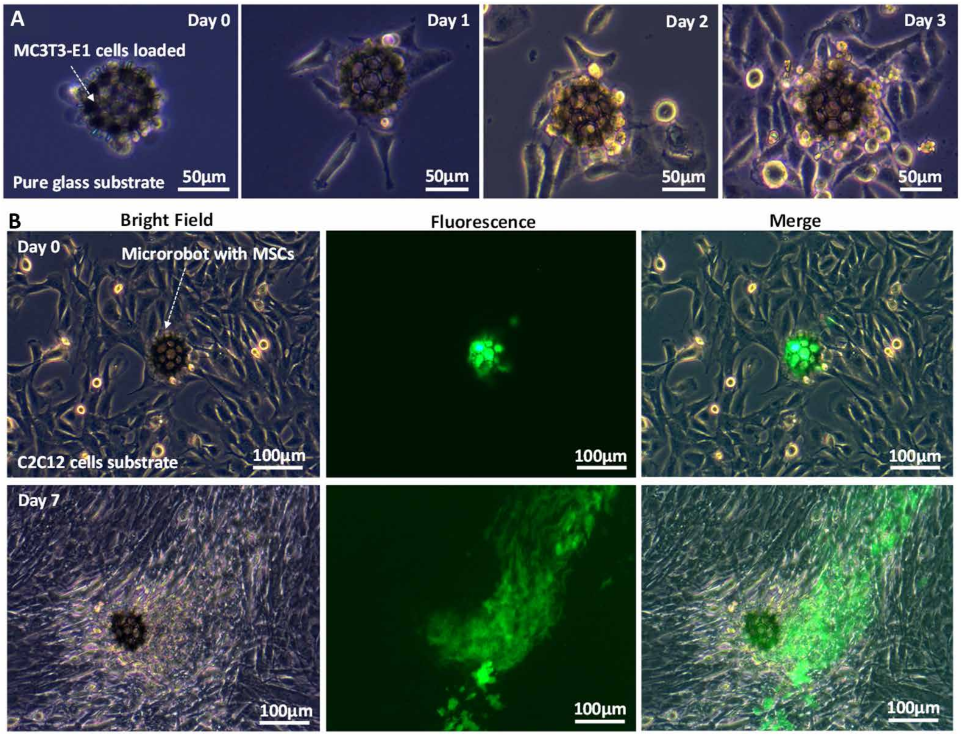

Fig. 6. In vitro cell-release experiments on a glass substrate. (**A**) MC3T3-E1 cells were released from the microrobot onto a pure glass substrate and proliferated at 3 days of cultivation. (**B**) MSCs transferred from the microrobot onto the glass substrate with precultured C2C12 cells at 7 days of cultivation.

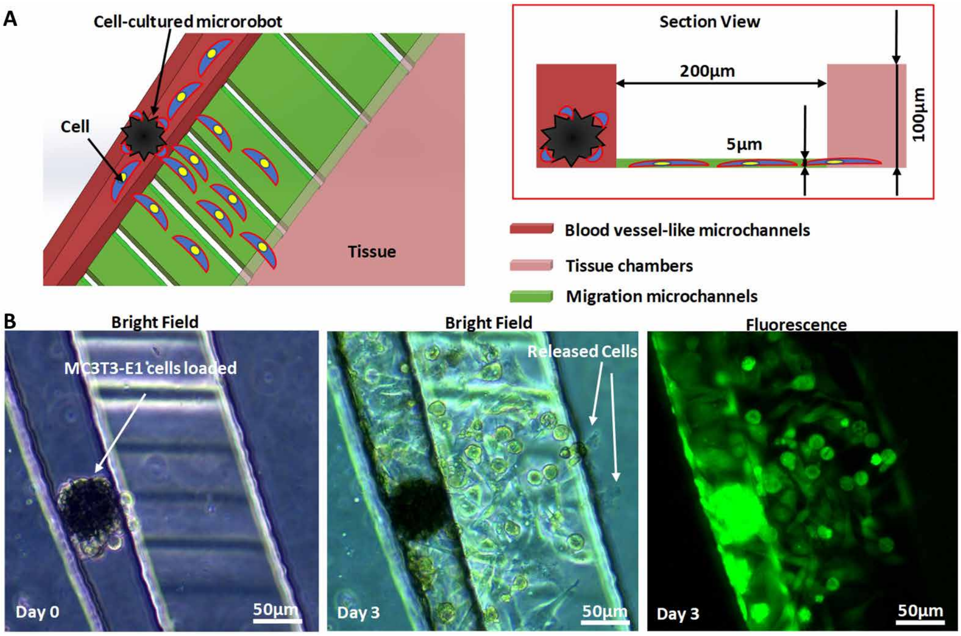

Fig. 7. In vitro cell-release experiments in a microfluidic chip. (**A**) Schematic of the cell-releasing process. (**B**) Results of the transendothelial migration of cells.

tissue area, indicating that the released cells could successfully pass the endothelial layer of blood vessel to reach the target area.

We lastly performed in vivo experiments on spontaneously releasing the cells from the microrobots to the site on nude mice. Because tumorigenic and tumor cells can be easily detected in weeks, we selected HeLa cells as sample cells to illustrate the in vivo releasing capacity of the microrobots. A swarm of microrobots carrying HeLa green fluorescent protein–positive (GFP^+) cells that were dispersed in 100 µl of PBS and 100 µl of Matrigel (1000 microrobots in 200 µl) was injected subcutaneously into the left dorsum of a nude mouse. The same amount of microrobots without HeLa cells was also injected into the right dorsum of the same mouse as a control. After 4 weeks of cultivation, an area with increased fluorescence intensity was observed at the left dorsum of the mouse (Fig. 8A), indicating that the tumor was due to the injected HeLa cells. No tumor was found at the right dorsum of the mouse after injection with microrobots without HeLa cells. To verify that the tumor was caused by the HeLa cells that were released from the microrobots to the surrounding tissues and not by the cells that stayed on the microrobots, we sacrificed the mouse after 4 weeks of injection to obtain the in vivo histological results (Fig. 8B). The microrobots, as indicated by the light micrographs in these sections, were all located at the edge of the tumor tissue, suggesting that the tumor was developed by the HeLa cells that were released from the injected microrobots onto the tissues.

DISCUSSIONS

This paper reports the design of a magnetic burr-like spherical porous microrobot for carrying and delivering targeted cells to a desired site in vivo under a magnetic gradient field–driven mechanism. The 3D laser lithography that was used to fabricate the microrobots provided sufficient flexibility to optimize the robot structure. Different cell types, including MC3T3-E1 cells and MSCs, were selected for the test. MC3T3-E1 cells can potentially differentiate into osteocytes. MSCs can potentially differentiate into various cell types of the host tissues, such as adipocytes, chondrocytes, and myocytes. Release of cells from the designed microrobots has been demonstrated through transferring cells onto glass substrates, mimicking the transendothelial migration of the released cells, and in vivo release of cells on nude mice. HeLa cells were used for the in vivo cell-release experiments because tumorigenic cells can generate tumor in weeks. The HeLa cells provided evidence that the cells

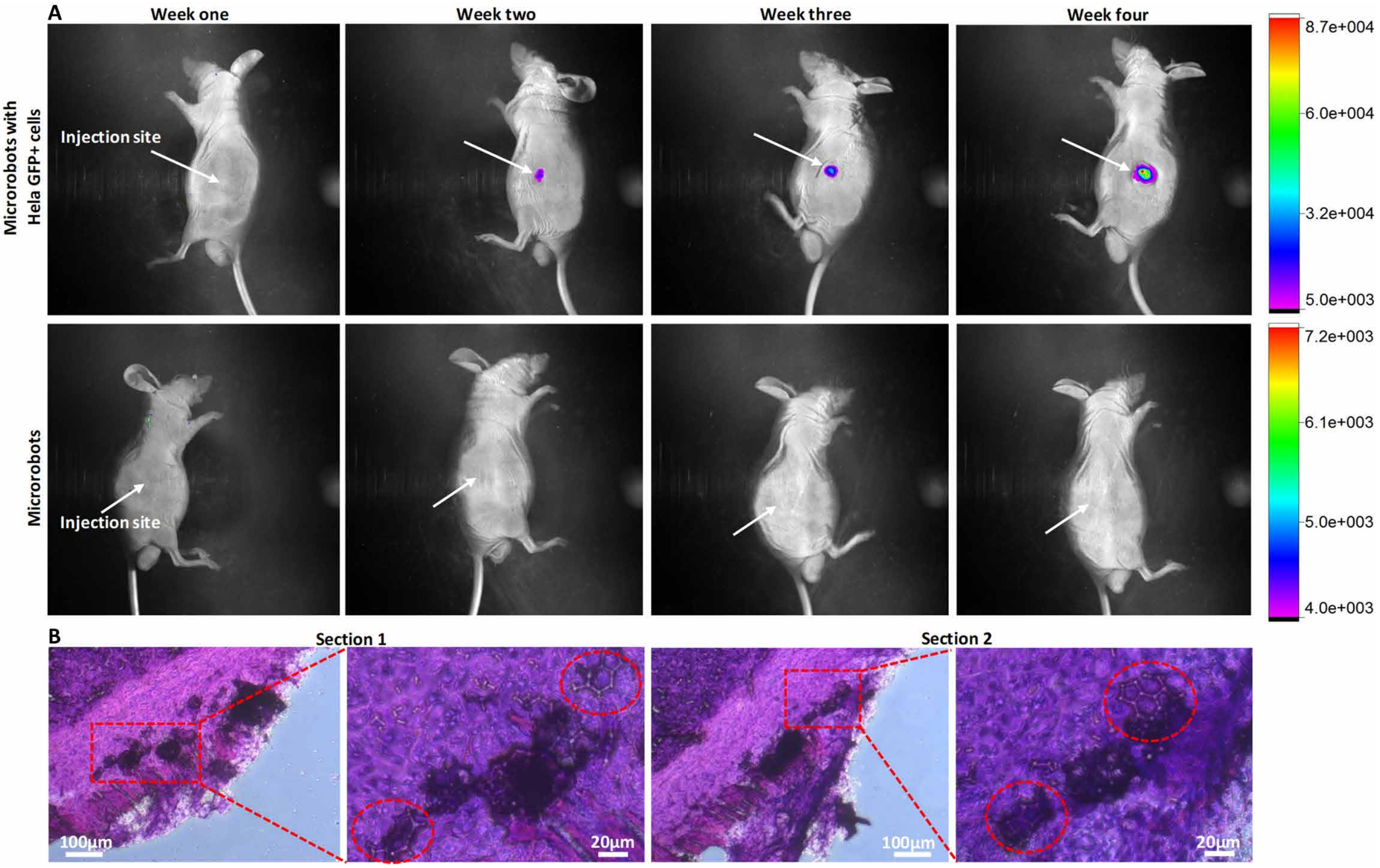

Fig. 8. In vivo cell-release experiments on nude mice. (**A**) In vivo fluorescence imaging of a swarm of microrobots. The microrobots with HeLa GFP$^+$ cells were injected into the left dorsum of the nude mice. The microrobots not carrying any cells were injected into the right dorsum of the nude mice. White arrows represent the position of the injection. (**B**) Two different hematoxylin-eosin–stained sections of HeLa tumor with the injected microrobots. The positions of the microrobots are marked by the red dashed lines.

were released from the microrobots in vivo. Automatic navigation of the cell-cultured microrobots was also demonstrated in zebrafish embryos. The above results support the feasibility of using magnetic-driven microrobots for the precise delivery of targeted cells in vivo.

In the current study, transparent zebrafish was used as the animal model so that the microrobot could be directly observed under an ordinary optical microscope. For in vivo research involving other animal models, an effective in vivo imaging technology that is applied to deep tissues would be required to enable online implementation of automated real-time tracking control of the microrobots. Another unaddressed issue is developing a 3D biodegradable structure with high mechanical strength. In the current study, the 3D magnetic robot was biocompatible but not biodegradable. Hydrogel is degradable but lacks mechanical strength. A magnetic microrobot requires a 3D structure with high mechanical strength to overcome the cell tensile force.

MATERIALS AND METHODS

Microrobot fabrication

The microrobots were fabricated using a negative photoresist SU-8 50 (MicroChem, USA). First, a 100-μm-thick SU-8 layer was spin-coated onto a cleaned glass wafer under a suitable spin speed. Second, the substrate was prebaked at 65°C for 10 min and then at 95°C for 30 min. The substrate was subsequently cooled down to room temperature. Third, the designed microrobot was written into the SU-8 photoresist by using a commercial two-photon direct writing system (Nanoscribe GmbH, Germany) with a 100× oil immersion objective (numerical aperture = 1.4 from Zeiss). For SU-8 photoresists, postbaking was conducted at 65°C for 1 min and at 95°C for 10 min. Propylene glycol methyl ether acetate (Sigma Chemical Company, USA) was used to develop the written structures and remove unpolymerized SU-8 for 20 min. Last, the robot samples were coated with Ni (100 nm) for magnetic actuation and Ti (20 nm) for biocompatibility using a Quorum Q150TS Dual Target Sputtering System (Quorum Technologies Inc., Canada). The Ni and Ti materials were 99.99% pure.

Apparatus

The morphology of the fabricated microrobots was observed under SEM (FE-SEM; FEI, Nova 450). The atom composition of the microrobot was characterized using an energy-dispersive spectrometer (Oxford Instruments, INCA) to determine the success of the coating process. Cell viability tests were conducted by using a flow cytometer (BD Biosciences, San Jose, CA) to confirm that both coating materials (Ni and Ti) were not cytotoxic to cells. Magnetic control experiments were performed by using a self-constructed magnetic coil system. The in vivo fluorescence images of nude mice were obtained by a

Bruker 3D In Vivo Xtreme X-ray Imaging System. Tissue sections for the histological study of nude mice were cut using a CryoStar NX70 (Thermo Fisher Scientific, Waltham, MA, USA).

Cell culture on microrobot

The fibroblast MC3T3-E1 cells and MSCs were maintained separately in Dulbecco's minimum essential medium (DMEM) (Gibco, catalog no. 11965-092) supplemented with 10% fetal bovine serum (FBS; Gibco, catalog no. 10270-106), penicillin (100 U/ml), and streptomycin (100 U/ml; Invitrogen, catalog no. 15240-062) at 37°C in a humidified atmosphere of 5% CO_2. The two cell types were subsequently trypsinized and resuspended at a concentration of 1×10^6 cells/ml for cell seeding. The microrobots were coated with poly-L-lysine (10 μg/ml; PLL) (Sigma Chemical Company, catalog no. P-7890) and then sterilized via ultraviolet irradiation for 30 min. PLL is a positively charged synthetic amino acid chain that has been widely used as a coating material to enhance cell attachment because cell surfaces are always negatively charged (*49*). Subsequently, MC3T3 cells and MSCs were seeded into two culture dishes containing the fabricated microrobots. Each dish with cells and microrobots was stored in an incubator at 37°C under a humidified atmosphere of 5% CO_2 for 12 hours. Last, the cell-cultured microrobot was detached by a home-designed micromanipulator (fig. S5) (*50*, *51*).

Cell viability tests

MC3T3-E1 cells and MSCs were seeded onto the substrate samples and incubated for 1, 3, or 5 days. Cells were harvested and adjusted to a density of 1×10^6 cells/100 μl into 1.5-ml tubes. After washing twice with 1 ml of PBS, the cells were resuspended in 1 ml of absolute ethanol at −20°C for 10 min and then washed again with 1 ml of PBS. Last, 1 ml of diluted PI (Thermo Fisher Scientific, catalog no. P1304MP) was added to the staining buffer (500 μg/ml), and then the cells were incubated for 15 min at room temperature for flow cytometric analysis.

Microfluidic chip fabrication

The microfluidic chip was fabricated using soft-lithography technology. A 4-inch-diameter silicon wafer was used as the substrate and spin-coated with a 5-μm-thick layer of negative photoresist SU-8 2007 (Microchem Corp.). After prebaking, exposure, postbaking, and development, an SU-8 mold for the cell migration microchannel was obtained. A 100-μm-thick layer of negative photoresist SU-8 2050 (Microchem Corp.) was spin-coated onto the same wafer, and the pattern for molding the blood vessel–like microchannels and tissue chambers was defined by the same process. Appropriate amounts of polydimethylsiloxane (PDMS) (Sylgard 184, Dow Corning) and curing agent were mixed at a ratio of 10:1 by weight and poured onto the two-layer SU-8 mold. Further, the mold with PDMS mixture was placed in a vacuum oven and baked at 70°C for 2 hours to remove air bubbles and cure the PDMS. Last, the cured PDMS microchannel was peeled off from the mold, punched at the inlet and outlets, and bonded with a clean glass substrate to form the chip.

Cell-releasing experiments from microrobots

Experiments involving the release of MC3T3-E1 cells from the microrobots onto a pure glass substrate were first performed. MC3T3-E1 cells were maintained in DMEM at 37°C in a humidified atmosphere with 5% CO_2 and trypsinized and resuspended at a concentration of 1×10^6 cells/ml. The cells (1×10^6 cells/ml) were then seeded onto the microrobot and maintained in DMEM for 12 hours. Thereafter, the microrobot was detached from the glass and moved into a pure glass substrate for 3 days of cultivation.

Second, MSCs were released from the microrobots onto a cell-cultured substrate. C2C12 mouse myoblasts obtained from American Type Culture Collection (ATCC; Manassas, VA) were precultured on the glass substrate (5×10^3/cm^2) for 12 hours. MSCs were maintained in α-MEM (Gibco, catalog no. 11900-073) supplemented with 10% FBS, penicillin (100 U/ml), and streptomycin (100 U/ml) at 37°C in a humidified atmosphere with 5% CO_2. The cells were trypsinized and resuspended at a concentration of 1×10^6 cells/ml. After seeding on the microrobot, the cells were stained with CFDA SE (Cell Proliferation Assay and Tracking Kit; Beyotime, Shanghai, China) to observe whether the cells transferred onto the substrate and subsequently differentiated. Last, the stained microrobot was moved to contact the glass substrate that was precultured with C2C12 cells for 7 days.

We then performed in vitro experiments involving the release of MC3T3-E1 cells from the microrobot in a microfluidic chip. MC3T3-E1 cells were maintained in DMEM at 37°C in a humidified atmosphere with 5% CO_2. The cells were trypsinized, resuspended at a concentration of 1×10^6 cells/ml, and seeded on the microrobot. Thereafter, the cell-cultured microrobot was injected into the inlet of the microfluidic chip. After the microrobots carrying cultured cells arrived in the docking area, the cells were released from the microrobots and passed through the mimicked endothelial layer.

To release the cells from the microrobots onto the nude mice in vivo, we maintained HeLa GFP$^+$ cells (ATCC, Manassas, VA) in DMEM at 37°C in a humidified atmosphere with 5% CO_2, and the cells were trypsinized and resuspended at a concentration of 1×10^6 cells/ml. A swarm of microrobots containing HeLa GFP$^+$ cells (1×10^6 cells/ml) was maintained in DMEM for 12 hours, detached from the glass, dispersed in 100 μl of PBS and 100 μl of Matrigel (BD Biosciences), and injected into the dorsum of a 6-week-old Balb/C nude mouse. After 4 weeks, the mouse was euthanized, and the tumor was immediately removed and sliced into 80-μm-thick tissue sections after cryothermal treatment. Hematoxylin-eosin staining was performed following the instructions of the manufacturer (Beyotime, Shanghai, China).

SUPPLEMENTARY MATERIALS

robotics.sciencemag.org/cgi/content/full/3/19/eaat8829/DC1

Text

Fig. S1. Energy-dispersive spectrometry spectra.

Fig. S2. Prototype of the magnetically actuated micromanipulation system consists of fixed DT4E-core identical electromagnetic coils.

Fig. S3. Insertion of the cell-cultured microrobot into the zebrafish embryo for in vivo transportation experiments.

Fig. S4. Velocities of the cell-cultured microrobot in different medium under different magnetic field gradients.

Fig. S5. A self-constructed microprobe platform for microoperation.

Table S1. The Reynolds numbers and related environmental parameters.

Movie S1. Design and fabrication of cell-cultured microrobot.

Movie S2. Transportation of cell-cultured microrobot in vitro and in the yolk of zebrafish embryo.

Movie S3. Cells releasing experiments in vitro and in nude mice.

REFERENCES AND NOTES

1. C. Doucet, I. Ernou, Y. Zhang, J.-R. Llense, L. Begot, X. Holy, J.-J. Lataillade, Platelet lysates promote mesenchymal stem cell expansion: A safety substitute for animal serum in cell-based therapy applications. *J. Cell. Physiol.* **205**, 228–236 (2005).

2. S. Dimmeler, J. Burchfield, A. M. Zeiher, Cell-based therapy of myocardial infarction. *Arterioscler. Thromb. Vasc. Biol.* **28**, 208–216 (2008).
3. S. Guven, P. Chen, F. Inci, S. Tasoglu, B. Erkmen, U. Demirci, Multiscale assembly for tissue engineering and regenerative medicine. *Trends Biotechnol.* **33**, 269–279 (2015).
4. S. Terai, T. Ishikawa, K. Omori, K. Aoyama, Y. Marumoto, Y. Urata, Y. Yokoyama, K. Uchida, T. Yamasaki, Y. Fujii, K. Okita, I. Sakaida, Improved liver function in patients with liver cirrhosis after autologous bone marrow cell infusion therapy. *Stem Cells* **24**, 2292–2298 (2006).
5. S. Llames, E. García, V. García, M. del Río, F. Larcher, J. L. Jorcano, E. López, P. Holguín, F. Miralles, J. Otero, A. Meana, Clinical results of an autologous engineered skin. *Cell Tissue Bank.* **7**, 47–53 (2006).
6. V. F. M. Segers, R. T. Lee, Stem-cell therapy for cardiac disease. *Nature* **451**, 937–942 (2008).
7. G. Q. Daley, D. T. Scadden, Prospects for stem cell-based therapy. *Cell* **132**, 544–548 (2008).
8. M. F. Pittenger, A. M. Mackay, S. C. Beck, R. K. Jaiswal, R. Douglas, J. D. Mosca, M. A. Moorman, D. W. Simonetti, S. Craig, D. R. Marshak, Multilineage potential of adult human mesenchymal stem cells. *Science* **284**, 143–147 (1999).
9. Y. S. Pek, A. C. Wan, J. Y. Ying, The effect of matrix stiffness on mesenchymal stem cell differentiation in a 3D thixotropic gel. *Biomaterials* **31**, 385–391 (2010).
10. J. W. Haycock, 3D cell culture: A review of current approaches and techniques. *Methods Mol. Biol.* **695**, 1–15 (2011).
11. B. H. Lee, H. Shirahama, M. H. Kim, J. H. Lee, N.-J. Cho, L. P. Tan, Colloidal templating of highly ordered gelatin methacryloyl-based hydrogel platforms for three-dimensional tissue analogues. *NPG Asia Mater.* **9**, e412 (2017).
12. S. Kim, F. Qiu, S. Kim, A. Ghanbari, C. Moon, L. Zhang, B. J. Nelson, H. Choi, Fabrication and characterization of magnetic microrobots for three-dimensional cell culture and targeted transportation. *Adv. Mater.* **25**, 5863–5868 (2013).
13. L. G. Griffith, G. Naughton, Tissue engineering—Current challenges and expanding opportunities. *Science* **295**, 1009–1014 (2002).
14. K. Wei, M. Zhu, Y. Sun, J. Xu, Q. Feng, S. Lin, T. Wu, J. Xu, F. Tian, J. Xia, G. Li, L. Bian, Robust biopolymeric supramolecular "Host−Guest Macromer" hydrogels reinforced by in situ formed multivalent nanoclusters for cartilage regeneration. *Macromolecules* **49**, 866–875 (2016).
15. X. Zhao, J. Kim, C. A. Cezar, N. Huebsch, K. Lee, K. Bouhadir, D. J. Mooney, Active scaffolds for on-demand drug and cell delivery. *Proc. Natl. Acad. Sci. U.S.A.* **108**, 67–72 (2011).
16. L. Cui, B. Liu, G. Liu, W. Zhang, L. Cen, J. Sun, S. Yin, W. Liu, Y. Cao, Repair of cranial bone defects with adipose derived stem cells and coral scaffold in a canine model. *Biomaterials* **28**, 5477–5486 (2007).
17. Q. Yang, J. Peng, Q. Guo, J. Huang, L. Zhang, J. Yao, F. Yang, S. Wang, W. Xu, A. Wang, S. Lu, A cartilage ECM-derived 3-D porous acellular matrix scaffold for in vivo cartilage tissue engineering with PKH26-labeled chondrogenic bone marrow-derived mesenchymal stem cells. *Biomaterials* **29**, 2378–2387 (2008).
18. B. Grigolo, L. Roseti, M. Fiorini, M. Fini, G. Giavaresi, N. N. Aldini, R. Giardino, A. Facchini, Transplantation of chondrocytes seeded on a hyaluronan derivative (Hyaff®-11) into cartilage defects in rabbits. *Biomaterials* **22**, 2417–2424 (2001).
19. M. Sitti, H. Ceylan, W. Hu, J. Giltinan, M. Turan, S. Yim, E. Diller, Biomedical applications of untethered mobile milli/microrobots. *Proc. IEEE* **103**, 205–224 (2015).
20. B. J. Nelson, I. K. Kaliakatsos, J. J. Abbott, Microrobots for minimally invasive medicine. *Annu. Rev. Biomed. Eng.* **12**, 55–85 (2010).
21. F. Ullrich, C. Bergeles, J. Pokki, O. Ergeneman, S. Erni, G. Chatzipirpiridis, S. Pané, C. Framme, B. J. Nelson, Mobility experiments with microrobots for minimally invasive intraocular surgery. *Invest. Ophthalmol. Vis. Sci.* **54**, 2853–2863 (2013).
22. K. B. Yesin, K. Vollmers, B. J. Nelson, Modeling and control of untethered biomicrorobots in a fluidic environment using electromagnetic fields. *Int. J. Robot. Res.* **25**, 527–536 (2006).
23. K. E. Peyer, L. Zhang, B. J. Nelson, Bio-inspired magnetic swimming microrobots for biomedical applications. *Nanoscale* **5**, 1259–1272 (2013).
24. J. J. Abbott, K. E. Peyer, M. C. Lagomarsino, L. Zhang, L. Dong, I. K. Kaliakatsos, B. J. Nelson, How should microrobots swim? *Int. J. Robot. Res.* **28**, 1434–1447 (2009).
25. A. Ghosh, P. Fischer, Controlled propulsion of artificial magnetic nanostructured propellers. *Nano Lett.* **9**, 2243–2245 (2009).
26. L. B. Zhao, L. Pan, K. Zhang, S. S. Guo, W. Liu, Y. Wang, Y. Chen, X. Z. Zhao, H. L. W. Chan, Generation of Janus alginate hydrogel particles with magnetic anisotropy for cell encapsulation. *Lab Chip* **9**, 2981–2986 (2009).
27. S. Tasoglu, E. Diller, S. Guven, M. Sitti, U. Demirci, Untethered micro-robotic coding of three-dimensional material composition. *Nat. Commun.* **5**, 3124 (2014).
28. E. B. Steager, M. Selman Sakar, C. Magee, M. Kennedy, A. Cowley, V. Kumar, Automated biomanipulation of single cells using magnetic microrobots. *Int. J. Robot. Res.* **32**, 346–359 (2013).
29. T.-Y. Huang, M. S. Sakar, A. Mao, A. J. Petruska, F. Qiu, X.-B. Chen, S. Kennedy, D. Mooney, B. J. Nelson, 3D printed microtransporters: Compound micromachines for spatiotemporally controlled delivery of therapeutic agents. *Adv. Mater.* **27**, 6644–6650 (2015).
30. S. Tottori, L. Zhang, F. Qiu, K. K. Krawczyk, A. Franco-Obregón, B. J. Nelson, Magnetic helical micromachines: Fabrication, controlled swimming, and cargo transport. *Adv. Mater.* **24**, 811–816 (2012).
31. M. Medina-Sánchez, L. Schwarz, A. K. Meyer, F. Hebenstreit, O. G. Schmidt, Cellular cargo delivery: Toward assisted fertilization by sperm-carrying micromotors. *Nano Lett.* **16**, 555–561 (2015).
32. X. Yan, Q. Zhou, M. Vincent, Y. Deng, J. Yu, J. Xu, T. Xu, T. Tang, L. Bian, Y.-X. Wang, K. Kostarelos, L. Zhang, Multifunctional biohybrid magnetite microrobots for imaging-guided therapy. *Sci. Robot.* **2**, eaaq1155 (2017).
33. W. Ma, J. Li, F. Niu, H. Ji, D. Sun, Robust control to manipulate a microparticle with electromagnetic coil system. *IEEE Trans. Ind. Electron.* **64**, 8566–8577 (2017).
34. G. J. Lieschke, P. D. Currie, Animal models of human disease: Zebrafish swim into view. *Nat. Rev. Genet.* **8**, 353–367 (2007).
35. K. Howe, M. D. Clark, C. F. Torroja, J. Torrance, C. Berthelot, M. Muffato, J. E. Collins, S. Humphray, K. McLaren, L. Matthews, S. McLaren, I. Sealy, M. Caccamo, C. Churcher, C. Scott, J. C. Barrett, R. Koch, G.-J. Rauch, S. White, W. Chow, B. Kilian, L. T. Quintais, J. A. Guerra-Assunção, Y. Zhou, Y. Gu, J. Yen, J.-H. Vogel, T. Eyre, S. Redmond, R. Banerjee, J. Chi, B. Fu, E. Langley, S. F. Maguire, G. K. Laird, D. Lloyd, E. Kenyon, S. Donaldson, H. Sehra, J. Almeida-King, J. Loveland, S. Trevanion, M. Jones, M. Quail, D. Willey, A. Hunt, J. Burton, S. Sims, K. McLay, B. Plumb, J. Davis, C. Clee, K. Oliver, R. Clark, C. Riddle, D. Elliott, G. Threadgold, G. Harden, D. Ware, S. Begum, B. Mortimore, G. Kerry, P. Heath, B. Phillimore, A. Tracey, N. Corby, M. Dunn, C. Johnson, J. Wood, S. Clark, S. Pelan, G. Griffiths, M. Smith, R. Glithero, P. Howden, N. Barker, C. Lloyd, C. Stevens, J. Harley, K. Holt, G. Panagiotidis, J. Lovell, H. Beasley, C. Henderson, D. Gordon, K. Auger, D. Wright, J. Collins, C. Raisen, L. Dyer, K. Leung, L. Robertson, K. Ambridge, D. Leongamornlert, S. McGuire, R. Gilderthorp, C. Griffiths, D. Manthravadi, S. Nichol, G. Barker, S. Whitehead, M. Kay, J. Brown, C. Murnane, E. Gray, M. Humphries, N. Sycamore, D. Barker, D. Saunders, J. Wallis, A. Babbage, S. Hammond, M. Mashreghi-Mohammadi, L. Barr, S. Martin, P. Wray, A. Ellington, N. Matthews, M. Ellwood, R. Woodmansey, G. Clark, J. D. Cooper, A. Tromans, D. Grafham, C. Skuce, R. Pandian, R. Andrews, E. Harrison, A. Kimberley, J. Garnett, N. Fosker, R. Hall, P. Garner, D. Kelly, C. Bird, S. Palmer, I. Gehring, A. Berger, C. M. Dooley, Z. Ersan-Ürün, C. Eser, H. Geiger, M. Geisler, L. Karotki, A. Kirn, J. Konantz, M. Konantz, M. Oberländer, S. Rudolph-Geiger, M. Teucke, C. Lanz, G. Raddatz, K. Osoegawa, B. Zhu, A. Rapp, S. Widaa, C. Langford, F. Yang, S. C. Schuster, N. P. Carter, J. Harrow, Z. Ning, J. Herrero, S. M. J. Searle, A. Enright, R. Geisler, R. H. A. Plasterk, C. Lee, M. Westerfield, P. J. de Jong, L. I. Zon, J. H. Postlethwait, C. Nüsslein-Volhard, T. J. P. Hubbard, H. Roest Crollius, J. Rogers, D. L. Stemple, The zebrafish reference genome sequence and its relationship to the human genome. *Nature* **496**, 498–503 (2013).
36. P. Danilevičius, R. A. Rezende, F. D. A. S. Pereira, A. Selimis, V. A. Kasyanov, P. Noritomi, J. L. L. da Silva, M. Chatzinikolaidou, M. Farsari, V. Mironov, Burr-like, laser-made 3D microscaffolds for tissue spheroid encagement. *Biointerphases* **10**, 021011 (2015).
37. V. Mironov, R. P. Visconti, V. Kasyanov, G. Forgacs, C. J. Drake, R. R. Markwald, Organ printing: Tissue spheroids as building blocks. *Biomaterials* **30**, 2164–2174 (2009).
38. H. Agrawal, H. Shang, A. P. Sattah, N. Yang, S. M. Peirce, A. J. Katz, Human adipose-derived stromal/stem cells demonstrate short-lived persistence after implantation in both an immunocompetent and an immunocompromised murine model. *Stem Cell Res. Ther.* **5**, 142 (2014).
39. F. Qiu, S. Fujita, R. Mhanna, L. Zhang, B. R. Simona, B. J. Nelson, Magnetic helical microswimmers functionalized with lipoplexes for targeted gene delivery. *Adv. Funct. Mater.* **25**, 1666–1671 (2015).
40. A. Altunbas, S. J. Lee, S. A. Rajasekaran, J. P. Schneider, D. J. Pochan, Encapsulation of curcumin in self-assembling peptide hydrogels as injectable drug delivery vehicles. *Biomaterials* **32**, 5906–5914 (2011).
41. C. Debbaut, P. Segers, P. Cornillie, C. Casteleyn, M. Dierick, W. Laleman, D. Monbaliu, Analyzing the human liver vascular architecture by combining vascular corrosion casting and micro-CT scanning: A feasibility study. *J. Anat.* **224**, 509–517 (2014).
42. A. Nakai, I. Sekiya, A. Oya, T. Koshino, T. Araki, Assessment of the hepatic arterial and portal venous blood flows during pregnancy with Doppler ultrasonography. *Arch. Gynecol. Obstet.* **266**, 25–29 (2002).
43. J. Rouwkema, N. C. Rivron, C. A. van Blitterswijk, Vascularization in tissue engineering. *Trends Biotechnol.* **26**, 434–441 (2008).
44. P. X. Ma, Biomimetic materials for tissue engineering. *Adv. Drug Deliv. Rev.* **60**, 184–198 (2008).
45. S. J. Hollister, Porous scaffold design for tissue engineering. *Nat. Mater.* **4**, 518–524 (2005).
46. T. Kawano, M. Sato, H. Yabu, M. Shimomura, Honeycomb-shaped surface topography induces differentiation of human mesenchymal stem cells (hMSCs): Uniform porous polymer scaffolds prepared by the breath figure technique. *Biomater. Sci.* **2**, 52–56 (2014).
47. H. Kim, J. Ali, U. K. Cheang, J. Jeong, J. S. Kim, M. J. Kim, Micro manipulation using magnetic microrobots. *J. Bionic Eng.* **13**, 515–524 (2016).

48. X. Li, C. Liu, S. Chen, Y. Wang, S. H. Cheng, D. Sun, In vivo manipulation of single biological cells with an optical tweezers-based manipulator and a disturbance compensation controller. *IEEE Trans. Robot.* **33**, 1200–1212 (2017).
49. D. Mazia, G. Schatten, W. Sale, Adhesion of cells to surfaces coated with polylysine. Applications to electron microscopy. *J. Cell Biol.* **66**, 198–200 (1975).
50. Y. T. Chow, S. Chen, C. Liu, C. Liu, L. Li, C. W. M. Kong, S. H. Cheng, R. A. Li, D. Sun, A high-throughput automated microinjection system for human cells with small size. *IEEE/ASME Trans. Mech.* **21**, 838–850 (2016).
51. Y. T. Chow, S. Chen, R. Wang, C. Liu, C.-w. Kong, R. A. Li, S. H. Cheng, D. Sun, Single cell transfection through precise microinjection with quantitatively controlled injection volumes. *Sci. Rep.* **6**, 24127 (2016).

Acknowledgments: We thank G. Li and group in the Chinese University of Hong Kong for supporting the MSCs and osteoblast-like MC3T3-E1 cells for this research, T. Huang in Peking University for the useful discussion on the fabrication of the designed microrobots, Y. Wang in City University of Hong Kong for supporting the animal tests, and W. Ma, Y.-t. Chow, and F. Niu in City University of Hong Kong for the useful discussion in magnetic manipulation experiments. **Funding:** This work was supported by grants from Research Grant Council of Hong Kong Special Administrative Region, China (project no. CityU 11267916 and CityU 11210315), and Shenzhen Science and Technology Project, China (project no. R-IND13301). **Author contributions:** D.S. proposed the idea and conceived the project. J.L., X.L., T.L., R.W., S.C., and D.S. designed and conducted the experiments, analyzed the data, and wrote the manuscript. D.L. assisted the magnetic control experiments. C.L. and S.C. assisted experiments on zebrafish. J.Y. assisted the experiments on mice. All authors reviewed and approved the manuscript. **Competing interests:** D.S. and J.L. filed a U.S. patent application (no. 15/702,462) for the microrobot design. All other authors declare that they have no competing interests. **Data and materials availability:** All data needed to evaluate the conclusions in the paper are present in the paper and/or Supplementary Materials. Contact D.S. for additional information.

Submitted 14 April 2018
Accepted 31 May 2018
Published 27 June 2018
10.1126/scirobotics.aat8829

Citation: J. Li, X. Li, T. Luo, R. Wang, C. Liu, S. Chen, D. Li, J. Yue, S.-h. Cheng, D. Sun, Development of a magnetic microrobot for carrying and delivering targeted cells. *Sci. Robot.* **3**, eaat8829 (2018).

Science Robotics

Development of a magnetic microrobot for carrying and delivering targeted cells

Junyang Li, Xiaojian Li, Tao Luo, Ran Wang, Chichi Liu, Shuxun Chen, Dongfang Li, Jianbo Yue, Shuk-han Cheng, and D. Sun

Sci. Robot. **3** (19), eaat8829. DOI: 10.1126/scirobotics.aat8829

Science Robotics (ISSN 2470-9476) is published by the American Association for the Advancement of Science. 1200 New York Avenue NW, Washington, DC 20005. The title *Science Robotics* is a registered trademark of AAAS.